中國機械工程學刊第三十九卷第二期第 131~143 頁(民國一百零七年)
Journal of the Chinese Society of Mechanical Engineers, Vol.39, No.2, pp 131~143 (2018)

Microstructure and Intergranular Corrosion Resistance Evaluation of Alloy 82 Weldments

Hwa-Teng Lee* and Te-Chen Liu**

Keywords: Alloy 82 weld, laser surface melting (LSM), intergranular corrosion (IGC), pitting corrosion

ABSTRACT

An investigation is performed into the grain boundary character distribution (GBCD), degree of sensitization (DOS), and intergranular corrosion (IGC) resistance of Alloy 82 overlay welds prepared using a manual gas tungsten arc welding (GTAW) process. Four different weldments are considered, namely as-welded (AW), sensitized (AW+SEN), solution-annealed (SS), and solution-annealed and then sensitized (SS+SEN). The results show that approximately 67.9% and 212.4 cm/cm^2 of the grain boundaries in the weldments were prepared by GTAW process found AW specimens are high-angle boundaries (>15°). These boundaries prompt the precipitation of fine Cr-carbides during sensitization treatment, and therefore cause the formation of Cr-depletion zones close to the grain boundary. Consequently, the AW+SEN weldment has a high DOS. By contrast, AW+SEN welds are processed using a laser surface melting (LSM) technique with a continuous CO_2 laser beam and scanning speeds in the range of 0.8~1.2 m/min. It is shown that the LSM treatment could improve IGC and pitting corrosion resistance of the overlay weld mainly by reducing the amounts of fine precipitates along the subgrain boundaries of sensitized weld.

Paper Received June, 2017. Revised July, 2017. Accepted July, 2017. Author for Correspondence: Hwa-Teng Lee.

**Prof. Dr.-Ing., Department of Mechanical Engineering, National Cheng Kung University, No.1, University Road, Tainan 701, Taiwan, R. O. China, Telephone: +886-6-2757575 ext.62154, E-mail : htlee@mail.ncku.edu.tw,*
**Corresponding author*

***.Graduate student, Department of Mechanical Engineering, National Cheng Kung University, No.1, University Road, Tainan 701, Taiwan, R. O. China, E-mail:ldc0928@gmail.com*

INTRODUCTION

Alloy 182/82 has been widely used for the fabrication of dissimilar metal welds (DMWs) between the low alloy steel reactor vessel nozzles and the stainless steel safe-ends or pipes in nuclear power plants. However, the thermal histories of the DMWs result in the formation of Cr-depletion zones at the grain boundaries (referred to as a sensitization effect), and therefore increases the susceptibility of the weld to intergranular corrosion (IGC), interdendritic stress corrosion cracking (IDSCC), intergranular stress corrosion cracking (IGSCC) and primary water stress corrosion cracking (PWSCC) following long-term operation (Celin and Tehovnik, 2011; Kasparova, 2000; Peng et al, 2003).

A lot of studies have reported that the degree of sensitization (DOS) of the weld depends strongly on the grain boundary character distribution (GBCD). In particular, the high DOS value is more prone to form along high-angle boundaries than low-angle boundaries (Lee and Wu, 2010; Lim et al, 2004). However, according to Hamada and Yamauchi (2003), the sensitization effect associated with fabrication and operation can be prevented if the alloys contain a sufficient amount of carbon-stabilizing elements such as Nb or Ti. For such alloys, the precipitation of NbC/TiC phases at high temperatures reduces the concentration of free carbon retained in the matrix to a low level, and therefore suppresses the precipitation of grain boundary Cr-rich carbides during PWHT. Furthermore, Sennour et al. (2013) showed that Alloy 82 welds containing a relatively greater amount of carbon (19 wt% Cr, 0.034 wt% C) are more likely to form $Cr_{23}C_6$ precipitates during heat treatment. As a result, Alloy 82 is particularly prone to IGC / IGSCC as a result of chromium depletion following heat treatment or long-term operation.

Alloy 82/182 welds are gradually being replaced with Alloy 52/52M welds in the fabrication of new nuclear power plants. However, the corrosion resistance of Alloy 182/82 is still an important concern since old nuclear power plants are expected to have an operational life of 60 years or more. Consequently, effective methods for improving the

corrosion resistance of Alloy 82 DMWs are urgently required in order to ensure the safety of the power plant. Alloy 82 welds are generally repaired using a tungsten inert gas (TIG) welding process, in which the alloy near the position of IGC or IGSCC is removed and an overlay weld is then prepared. However, the length of time needed to effect the repair, together with the high heat input, limits the practicality of the TIG welding technique for such applications(McCracken and Smith, 2011; Chu et al, 2013).

The use of laser surface melting (LSM) to improve the corrosion resistance of alloy welds has attracted growing interest in recent years. LSM is a high energy density process with a low heating effect. Therefore, it prompts a localized melting and re-solidification of the weld surface without affecting the mechanical properties of the other regions. Many studies have demonstrated the effectiveness of LSM in improving the IGC/IGSCC resistance of sensitized austenitic stainless steel and Alloy 600 (U.K. Mudali et al, 1991; Lim et al, 1997, 2001; Shin et al, 1998; Suh et al, 1998). In particular, it has been shown that the high temperature gradient associated with LSM results in a rapid solidification rate, which suppresses the precipitation of Cr-rich carbides at the grain boundaries and hence minimizes the number of potential sites for IGC/IGSCC initiation. Several studies have shown the potential of LSM for improving the stress corrosion cracking (SCC) resistance of Alloy 182 (Bao et al, 2006, 2009). However, the applicability of LSM to Alloy 82 welds has yet to be reported.

Accordingly, the present study performs a systematic investigation into GBCD, elemental composition, DOS and IGC resistance properties of Alloy 82 overlay welds prepared using a manual gas tungsten arc welding (GTAW) process. Four different weld conditions are considered, namely as-welded, solution-annealed, as-welded then sensitized, and solution-annealed and then sensitized. Having examined the IGC properties of the various welds, a further investigation is performed to explore the feasibility for improving the corrosion resistance of sensitized Alloy 82 welds through LSM treatment with a continuous CO_2 laser beam and various scanning speeds.

Experimental Procedures and Method

Alloy 82 metal was produced by Tientai Electrode Co., Ltd. in the form of wire (AWS A5.14 ERNiCr-3) with an outer diameter of 2.4 mm. Overlay welds with a thickness of 4 mm were prepared on 316L stainless steel substrates with dimensions of 80 mm × 50 mm × 6 mm using a three-pass GTAW process with welding currents ranging from 120~130 A, voltages of 14~15 V DC, and welding speeds of 1.9~2.4 mm/min. The chemical compositions of the weld metal and overlay weld are shown in Table 1. It is noted that both compositions are within specification.

The as-welded plates were designated as AW. They were solution-annealed at 1050℃ for 30 min and then quenched in water. The solution-annealed plates were designated as SS. The AS and SS plates were both sensitized at 650℃ for 24 hours with the heating and cooling rates of 10℃/hour. They were designated as AW+SEN and SS+SEN, respectively.

The AW+SEN plates were then processed by LSM treatment. Prior to surface modification, the specimens were grounded with 600-grit SiC abrasive paper in order to enhance the absorption of the laser beam energy. The LSM process was performed using a continuous CO_2 laser system with an output power of 4.8 kW, and a laser spot size of 10 mm. The scanning speeds were set to 0.8, 1.0 and 1.2 m/min. To prevent oxidization, the LSM process was performed in He shielding gas with a flow rate of 20 l/min. Moreover, the weld beads produced in each pass were offset by a distance of 5 mm from one another in order to increase the size of the treatment area (Lim et al, 2001; Bao et al, 2006). Figure 1 presents schematic illustrations of the GTAW and LSM processes (Lee and Liu, 2017).

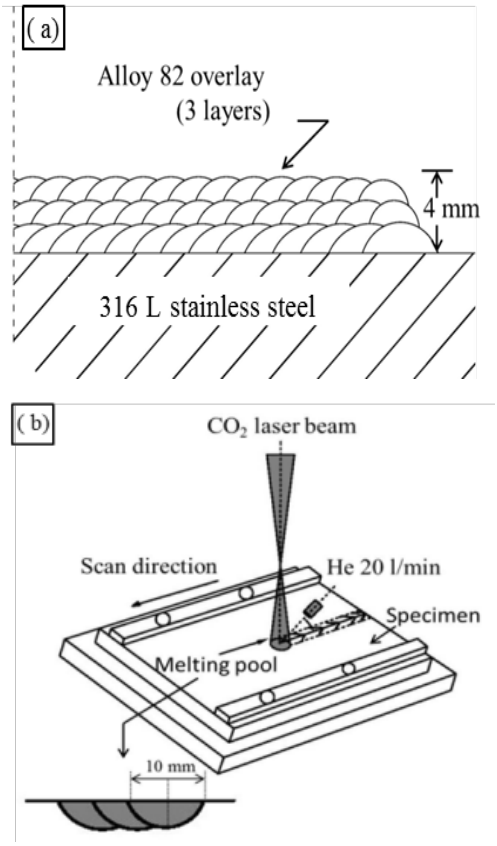

Fig. 1 Schematic illustrations of: (a) GTAW overlay welding process; (b) LSM treatment of overlay weld (Lee and Liu, 2017).

Table 1. Chemical compositions of filler metal and overlay weld (wt%).

Elements	C	Mn	Fe	P	S	Si	Cu	Ni	Co	Ti	Cr	Nb+Ta
Specification	Max	2.5	Max	Max	Max	Max	Max	Min	Max	Max	18.0	2.0
Requirements	0.10	3.5	3.0	0.03	0.015	0.50	0.50	57.0	0.12	0.75	22.0	3.0
Filler Metal	0.035	3.01	1.30	0.003	0.001	0.08	0.01	72.50	0.04	0.36	20.04	2.41
Overlay Weld*	0.04	2.82	1.86	0.004	0.002	0.04	0.01	71.52	0.05	0.34	20.46	2.69

*measured using optical emission spectrometer.

Test coupons with dimensions of 10 mm × 10 mm (length x width) were cut from the various plates using an electrical discharge machining wire cutter. The microstructures of the horizontal surfaces were characterized via optical microscopy (OM), electron backscattered diffraction (EBSD), scanning electron microscopy (SEM), and transmission electron microscopy (TEM). Prior to observation, the specimens were etched in a solution of 88% phosphoric acid (H_3PO_4) under a potential of 3 V for 30 s. For each specimen, the precipitates and segregation distribution of the alloying elements were analyzed by energy dispersive spectroscopy (EDS) and electron probe microanalysis (EPMA), respectively. Thin foil specimens for TEM observations were prepared using a double-jet thinner with 10% perchloric acid ($HClO_4$) at -10℃ and an agitation voltage of 20 V.

The IGC resistance properties of the various specimens were evaluated by means of double-loop electrochemical potentiodynamic reactivation (DL-EPR) and potentiostatic corrosion tests performed at room temperature. For each sample, the tests were performed with a scanning rate of 0.5 mV/s in a 0.05 M H_2SO_4 solution containing 0.003 M CH_3CSNH_2. (Note that CH_3CSNH_2 was deliberately chosen as the activator for the corrosion tests since previous studies have shown that the addition of potassium thiocyanate (KSCN) to H_2SO_4 solution can corrode the matrix to such an extent that the DOS of the alloy cannot be reliably determined (Tsai, et al, 2005; Liu et al, 1992; Fang et al, 1995). For each specimen, the DOS was evaluated as the ratio of the maximum anodic current in the reverse scanning curve to that in the forward scanning curve (i.e., DOS=Ir/Ia). Following the corrosion tests, the surface morphologies of the specimens were examined microscopically in order to determine the intrinsic corrosion mechanism.

RESULTS AND DISCUSSION

Effect of heat treatment on grain boundary microstructures

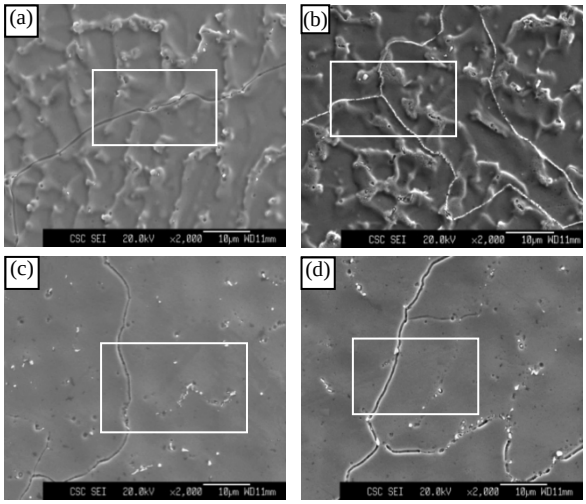

Fig. 2 SEM micrographs showing surface morphologies of: (a) AW specimen; (b) AW+SEN specimen; (c) SS specimen; (d) SS+SEN specimen.

Figure 2 presents SEM images of the etched surface morphologies of the AW, AW+SEN, SS and SS+SEN specimens. As shown in Figs. 2a and 2b, the microstructure of AW and AW+SEN specimens are similar. The sub-grain structure of both samples is primarily dendritic with interdendritic constituents formed through constitutional supercooling during the welding process. By contrast, the interdendritic microstructure of SS and SS+SEN specimens are not obvious. (see Figs. 2c and 2d). It can be attributed to the solution annealing that could eliminate the non-uniformity of the chemical composition in interdendritic regions and makes a stable passive film when performing electrochemical etching. Figs. 2a and 2b also reveal the presence of small white particles in the intragranular regions of the AW and AW+SEN samples. Moreover, the continuous precipitates are decorated along the grain boundaries in the AW+SEN sample (Fig. 2b). The SS sample (solutionized at 1050℃ for 0.5 h) contains a relatively larger number of white particles in the intragranular area than the AW sample (Fig. 2c). However, in contrast to the AW+SEN sample, the sensitization process does not induce the formation of continuous precipitates along the grain boundaries in

the SS+SEN sample (Fig. 2d).

The inverse pole figure (IPF) and grain boundary maps of the AW and SS samples are shown in Figure 3. Those maps were analyzed for the samples taken from the top surface of overlay welds. The NiCrFe austenitic phase data were used for phase construction in every case. The results indicate that all of the overlay welds have an austenitic matrix. During the solidification, the each dendrite tends to grow along <100> directions preferentially. Thus, the grains in the AW sample are aligned predominantly in the <100> direction (Fig. 3a-left) (Sindo Kou, 2003). By contrast, the trend of oriented grains in the <100> direction is reduced after solutionization (Fig. 3a-right). The intensity of the red color in the contour plot of the AW sample corresponds to a value around 5.7 times higher than that of the random background. For the SS sample, the intensity of the red color is reduced to around 4.5 times that of the random background. In other words, the solutionization process gradually transforms the microstructure of the AW weld from an isotropic structure to an anisotropic structure. However, it is still seen that the (100) pole is strongly aligned.

The grain boundary maps presented in Fig. 3b show that for both samples, the majority of the subgrain boundaries have a high orientation angle (i.e., 15~62.8°) For example, the detailed analysis results presented in Table 2 show that 67.9% of the subgrain boundaries in the AW specimen are high-angle boundaries (>15°), while 64.6% of those in the SS specimen are high-angle boundaries. Moreover, the densities of the high-angle boundaries in the AW and SS specimens are around 212.4 cm/cm^2 and 185.3cm/cm^2, respectively. The difference between the two values implies that the solutionization process has a significant effect on the pre-existing high-angle boundaries in the AW specimen. Thus, the solution-annealed structure accounts for the more uniform grain structure of SS specimen, as compared to the AW specimen. The grain boundary maps shown in Fig. 3b demonstrate the same trend of variation in grain size in distinct samples as the IPF maps shown in Fig. 3a. Solutionization causes the growth of numerous subgrains in the SS sample.

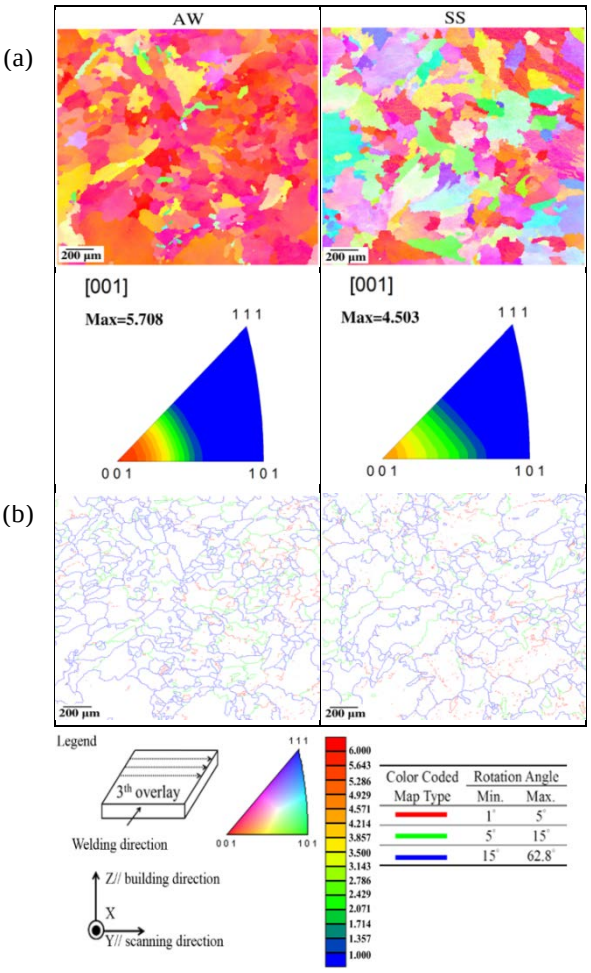

Fig. 3 EBSD results for AW and SS specimens: (a) IPF maps; (b) grain boundary maps (Lee and Liu, 2017).

Figure 4 shows the EPMA results for the elemental compositions of the AWand SS specimens. Figs. 4a presents high-magnification SEM images of the boxed regions in Figs. 2a and 2c, respectively, while Figs. 4b-e show the Cr, C, Nb and Ti distributions in the two samples. The mapping results show a distinct enrichment of C, Nb and Ti, and a distinct depletion of Cr, in the interdendritic regions of the AW specimen (see Figs. 4b). In other words, C, Nb and Ti elements are rejected into the interdendritic liquid during the post-welding solidification process.

Table 2. Grain boundary misorientation statistics for AW and SS specimens.

Rotation angle		AW			SS		
Min.	Max.	Length (cm)	Fraction (%)	Density (cm/cm^2)	Length (cm)	Fraction (%)	Density (cm/cm^2)
2°	5°	1.34	13.3	41.7	1.63	17.7	50.7
5°	15°	1.89	18.8	58.8	1.64	17.8	51.0
15°	62.8°	6.83	67.9	212.4	5.96	64.5	185.3

However, for the SS sample, no significant enrichment or depletion of Cr, C, Nb and Ti is observed, other than in the immediate vicinity of the white particles (see Figs. 4b-e). The white particles are rich in Nb and Ti, and hence it is inferred that the particles are (Nb.Ti)-rich carbides. It is therefore reasonable to suppose that the Nb and Ti elements rejected into the interdendritic regions during the original welding process subsequently combine with the free C in the matrix to form (Nb,Ti)-rich carbides during the solution-annealed process.

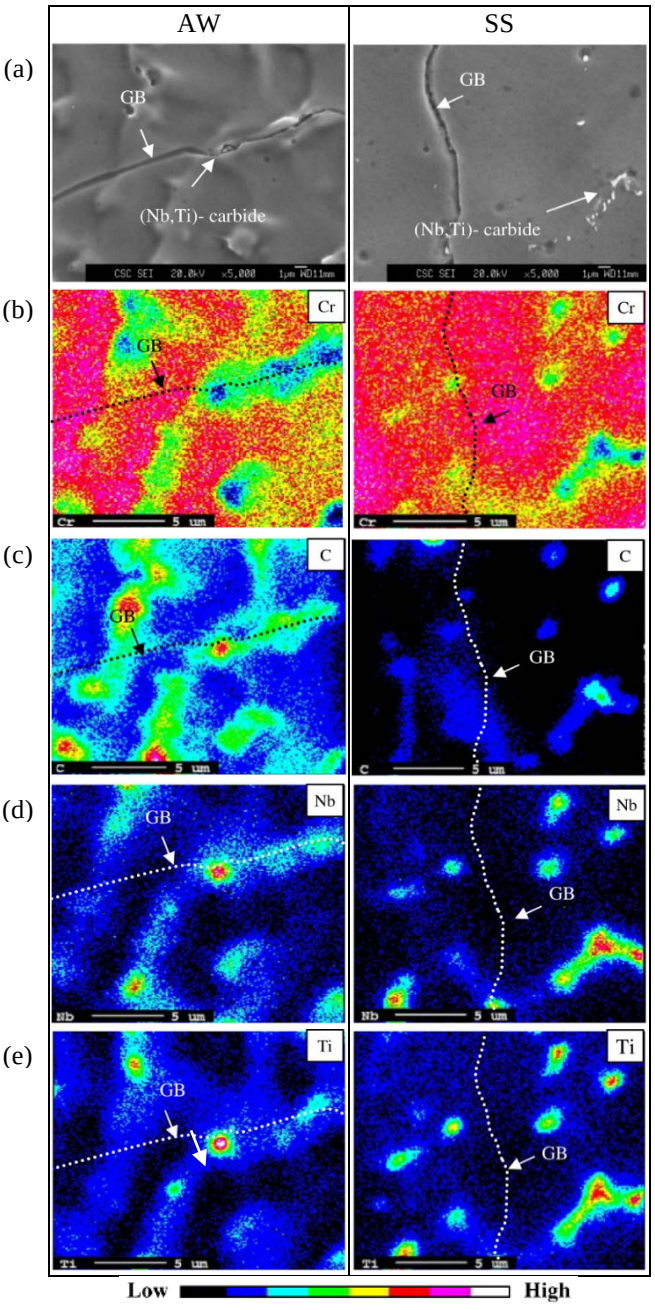

Fig. 4 EPMA results for AW and SS specimens: (a) SEM images; (b)-(e) Cr, C, Nb and Ti element mappings in (a), respectively (Lee and Liu, 2017).

Figure 5 shows the EPMA results for the AW+SEN and SS+SEN specimens. As discussed above, the AW (67.9%) and SS (64.6%) specimens have a similar fraction of high-angle boundaries. However, the EPMA results show that the two samples have a quite different grain boundary character distribution. For example, the grain boundaries of the SS+SEN sample are quite clean and have a uniform Cr, C, Nb and Ti distribution (see Figs. 5b-e). The uniform microstructure and elemental distribution suggests that the (Nb.Ti)-rich carbide precipitates in the SS sample reduce the concentration of free carbon retained in the matrix to such a level that no further precipitation of Cr-rich carbides along the grain boundaries is possible during the sensitization treatment. By contrast, the sensitized AW specimen shows a continuous morphology along the grain boundaries (see Fig. 5a). The C mapping results show that the C distribution along the grain boundary is nearly continuous (see Fig. 5c), which suggests the precipitation of C-rich carbides at the grain boundary. The mapping results in Figs. 5d and 5e indicate that these carbides are rich in Nb and Ti. Furthermore, the AW+SEN specimen shows a distinct depletion of Cr in the grain boundary region (see Fig. 5b). In other words, it is inferred that the sensitization treatment prompts the precipitation of Cr-carbides near the grain boundaries.

Figure 6 presents TEM micrographs of the AW+SEN specimen. The images in Figs. 6a and 6b show a near continuous distribution of precipitates, both large and small, along the grain boundary. The EDS analysis results show that the particles fall into two main types, namely (1) relatively large particles rich in Nb and containing traces of Ti and C (see Fig. 6c) and (2) fine particles rich in Cr and Ni and containing traces of Nb and C (see Fig. 6d). Nb and Ti both have a higher affinity for C than Cr. Hence, it is reasonable to assume that the particles which precipitate during the overlay welding process suppress the formation of Cr-rich particles. Moreover, according to the previous studies (Sennour et al, 2013; Briant and Hall, 1987), the fine-sized precipitates are likely to be $Cr_{23}C_6$ phases formed at the high-angle grain boundaries due to the high C content (0.035 wt% C) of the current filler metal.

Effect of heat treatment on IGC resistance

Figure 7 shows the DL-EPR curves of the AW, AW+SEN, SS and SS+SEN specimens. It is seen that the AW, SS and SS+SEN specimens experience no anodic dissolution during the reactivation scan. Thus, the DOS value is equal to zero in every case, and all the grain boundary regions and grain interior regions remain passivated. However, for the AW+SEN specimen, a high anodic current density is produced during reactivation. The DOS is estimated to be

approximately 31%. In other words, the weld has a high degree of sensitization (Cihal, 1980). Of the four samples, the SS specimen has the lowest passive current and corrosion potential. In other words, the solution treatment yields an effective improvement in the corrosion resistance of the original Alloy 82 weld. In summary, the results obtained in this study suggest that the SS specimen has a low DOS due to its high Cr content and the presence of Nb-Ti carbides, which suppress the formation of Cr-depletion zones.

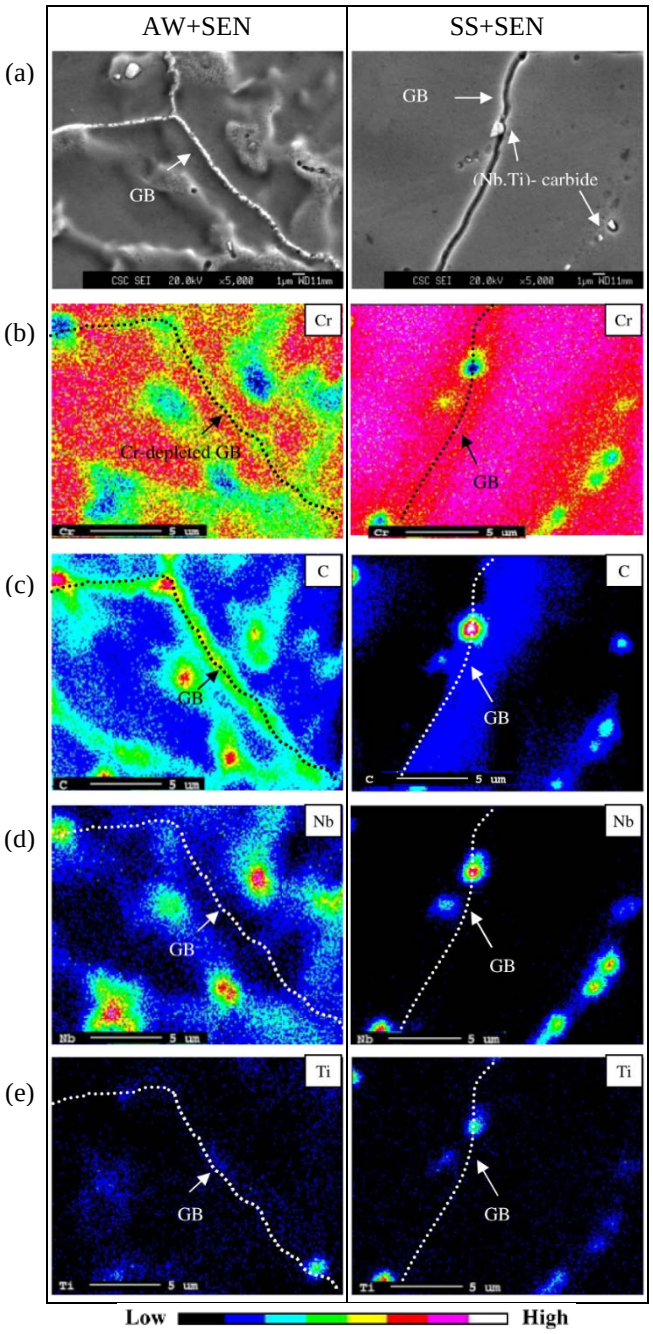

Fig. 5 EPMA results for AW+SEN and SS+SEN specimens: (a) SEM images; (b)-(e) Cr, C, Nb and Ti element mappings in (a), respectively(Lee and Liu, 2017).

Furthermore, the EBSD analysis results suggest that the improved resistance of the SS specimen stems mainly from a reduction in the fraction and density of high-angle grain boundaries compared to that in the AW sample.

Figure 8 presents optical micrographs of the specimen surfaces following the DL-EPR tests. The AW+SEN specimen shows evidence of extensive IGC and pitting corrosion (see Fig. 8b). By contrast, the AW, SS and SS+SEN specimens show only mild corrosion. Therefore, it can be inferred that the high anodic reactivation current density of the AW+SEN specimen shown in Fig. 7 is most likely the result of IGC and pitting corrosion.

Figure 9 shows the EPMA results for the AW+SEN sample. The C mapping results show evidence of C enrichment along the corrosion tunnels on the sample surface (see Fig. 9c). Furthermore, the Cr mapping results (Fig. 9b) show that the corrosion tunnels contain both Cr-rich zones (indicated in red) and Cr-depleted zones (indicated in blue). As shown in Fig. 9d, the Cr-depleted zones are rich in Nb, and thus most likely correspond to positions occupied by (Nb,Ti)-rich carbides. Similarly, the Cr-rich zones most likely to correspond to the positions of Cr-rich carbides.

Figure 10 presents the detailed EPMA results for the boxed region of the SEM image in Fig. 9. The mapping results show a high Cr content in the center of the corrosion tunnel and a low Cr content close to the walls. Consequently, it appears that the IGC mechanism is the result of a two-fold microgalvanic coupling process involving (1) galvanic coupling between the (Nb,Ti)-rich carbides and the adjacent matrix, and (2) galvanic coupling between the Cr-rich zones at the grain boundaries and the adjacent matrix. In other words, the IGC of the sensitized Alloy 82 weld is caused not by the anodic dissolution of the grain boundary itself, but by the anodic dissolution of the adjacent matrix in the vicinity of the Cr- depleted zones.

Figure 11a presents a backscattered electron image (BEI) of the corroded AW+SEN surface shown in Fig 9a. As shown, pitting occurred within the grains. Moreover, several bright contrast particles are observed within the pitting hole and on the walls of the corrosion tunnel (see Fig. 11b). The EDS analysis results show that the smaller of the two particles is rich in Nb and has traces of C and Ti (see Fig. 11c), while the larger particle is rich in Nb and Ti and has traces of C (see Fig. 11d). The EPMA results in Figs. 9 and 10 show evidence of Cr-depletion in the vicinity of these (Nb,Ti)-rich particles. Due to the high nobility of (Nb,Ti)-rich particles(Lee and Kuo, 1999; Lee and Jeng, 2001), the pitting corrosion susceptibility of the AW+SEN sample can be attributed mainly to galvanic coupling between these particles and the adjacent matrix.

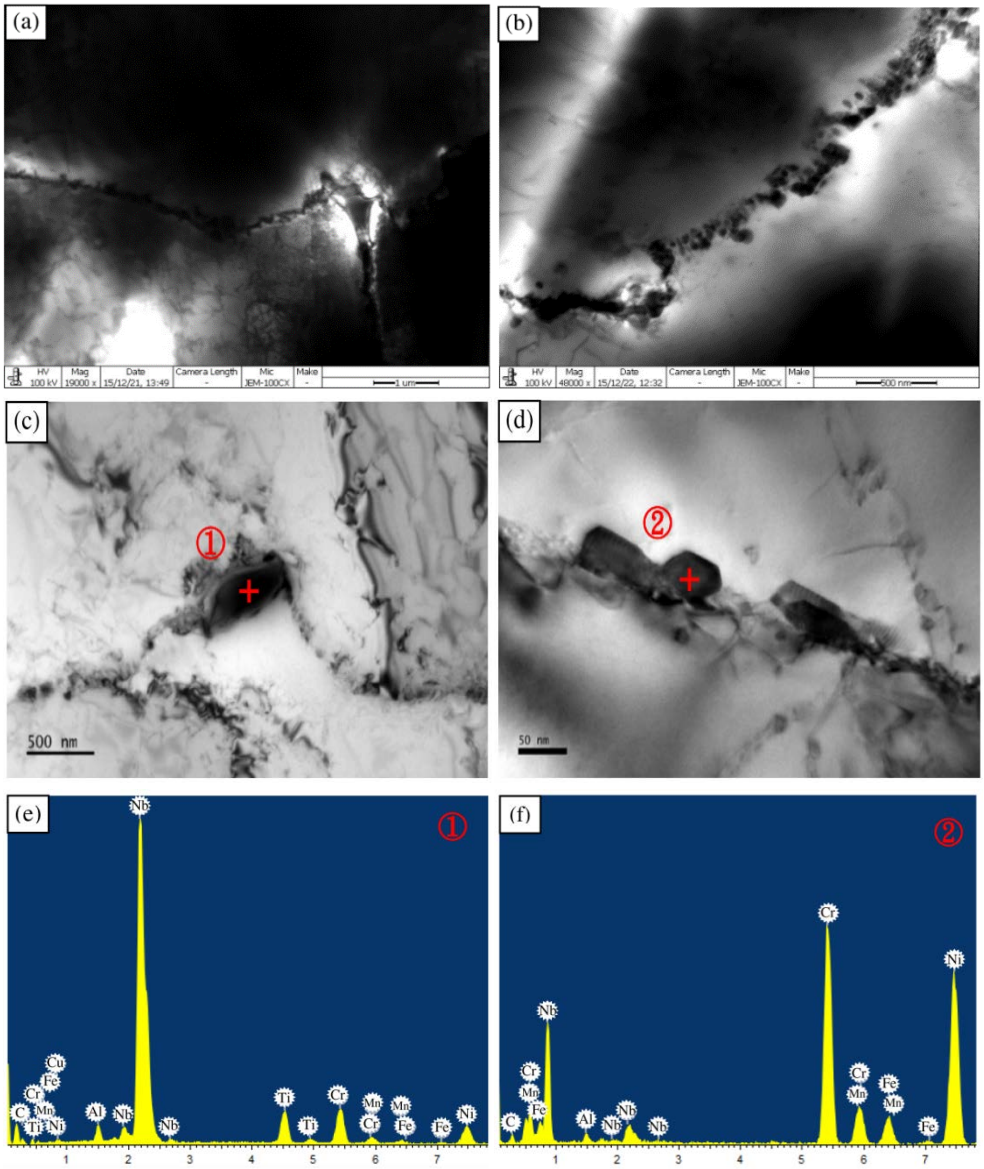

Fig. 6 TEM micrographs and EDS analysis results for large (Nb,Ti)-rich carbides and fine Cr-rich carbides in AW+SEN specimen: (a),(b) TEM images of precipitates at grain boundaries; (c),(d) High-magnification TEM images of precipitates; (e),(f) EDS analysis results for (Nb,Ti)-rich carbides in (c) and Cr-rich carbides in (d).

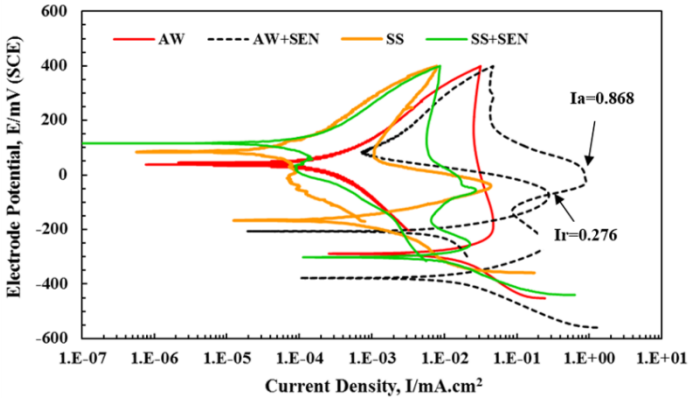

Fig. 7 DL-EPR polarization curves for AW, AW+SEN, SS and SS+SEN specimens.

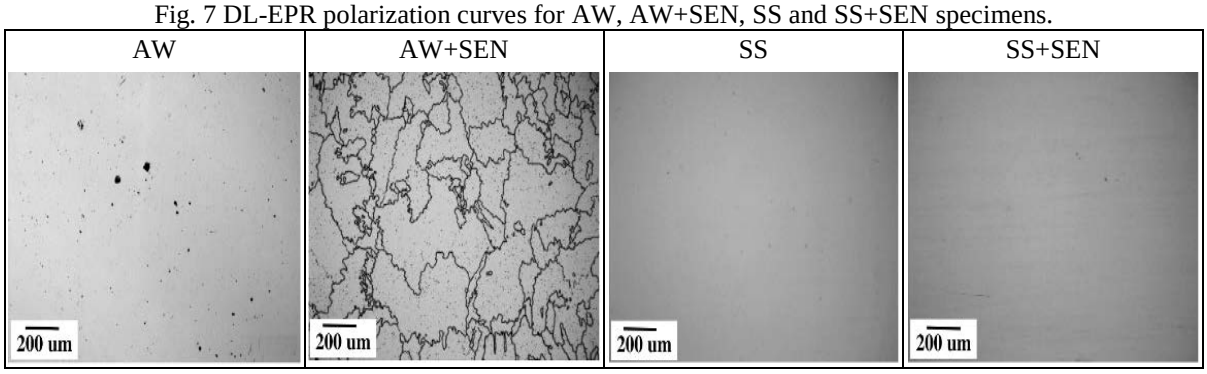

Fig. 8 Optical photographs of AW, AW+SEN, SS and SS+SEN specimens after DL-EPR tests.

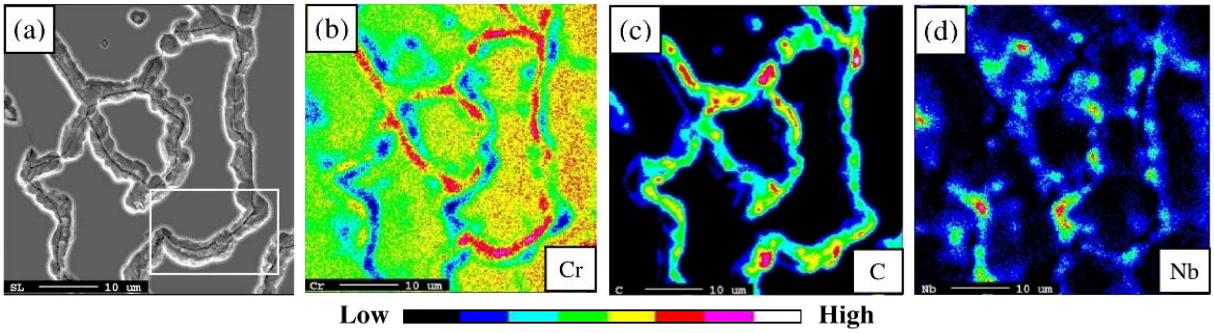

Fig. 9 EPMA results for corroded surface of AW+SEN specimen after DL-EPR test: (a) SEM image; (b)-(d) Cr, C and Nb element mappings, respectively.

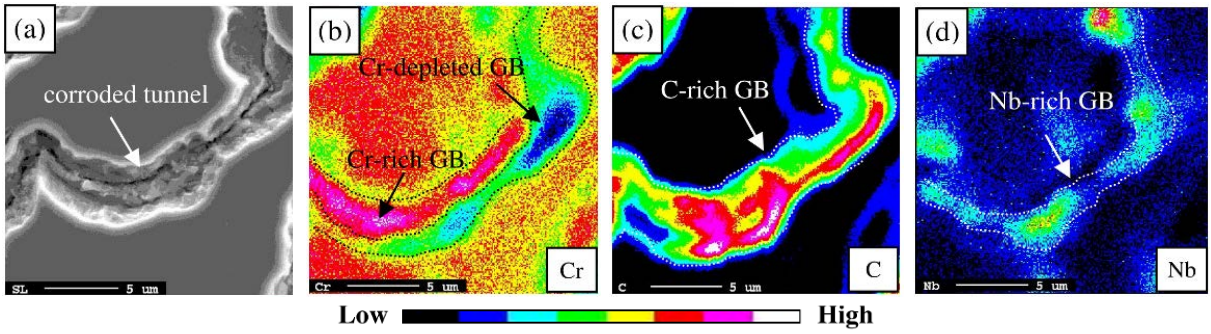

Fig. 10 EPMA results for corroded tunnel shown in boxed region of Fig. 9: (a) SEM image; (b)-(d) Cr, C and Nb element mappings, respectively.

Effect of LSM treatment on IGC resistance

Figure 12 presents cross-sectional micrographs of the AW+SEM samples following LSM treatment with three different scanning speeds. For each sample, the microstructure contains two distinct zones, namely a laser-melted zone (LMZ) and an unaffected zone. From inspection, the LMZ depth is increased with the decrease of scanning speed, equal to 240~250 μm, 160~170 μm and 150~160 μm in the LSM-0.8, LSM-1.0 and LSM-1.2 samples, respectively. For each sample, the LMZ microstructure consists of a thin upper layer of fine cellular dendrite and a lower layer of columnar dendrite. The upper layer has a thickness of approximately 50~60 μm, 30~40 μm and 14~18 μm in the LSM-0.8, LSM-1.0 and LSM-1.2 samples, respectively, and is a result of the different laser power given a different scanning speed. It is observed that the dendritic spacing of the columnar dendrite layer is significantly smaller than that of the unaffected zone due to the effects of the rapid cooling rate following the LSM process.

Figure 13 shows the EPMA results for the

LSM-0.8 sample. (Note that the sample is chosen arbitrarily here for illustration purposes.) For each image, the upper region corresponds to the LMZ, while the lower region corresponds to the unaffected zone. The SEM image shows that the LSM treatment results in a significant reduction in the number of interdendritic precipitates (see Fig. 13a, LMZ zone). In other words, it appears that the LSM process prompts the dissolution of the precipitates into the matrix, and thus results in a more homogeneous microstructure. This inference is reasonable since, in the LSM process, the peak temperature in the melted pool possibly exceeds 1240℃ (Lee and Wu, 2010) and is thus sufficiently high to decompose the Cr-carbides. Due to the concentration difference between the Cr-carbides and the matrix, the Cr atoms diffuse into the matrix while in the liquid state. Consequently, both the Cr-carbide precipitates and the Cr-depletion zones are eliminated in the LSM specimen.

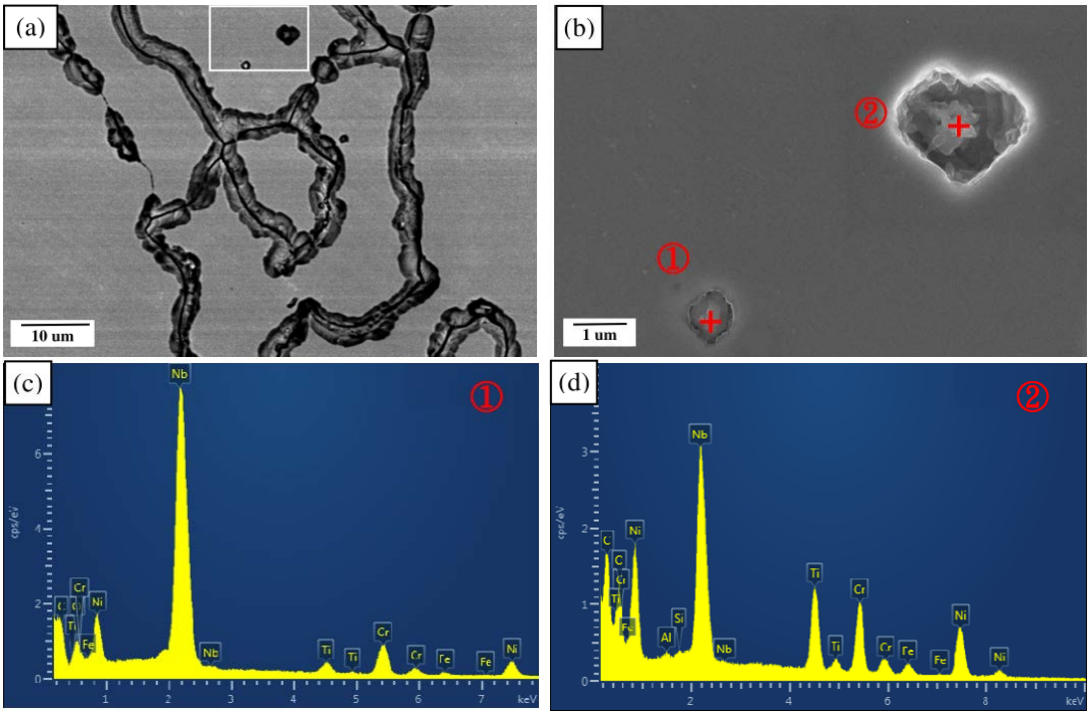

Fig. 11 (a) Backscattered electron image of corroded tunnel in Fig. 9(a); (b) SEM image of precipitates in pitting holes; (c),(d) EDS analysis results for precipitates in (b).

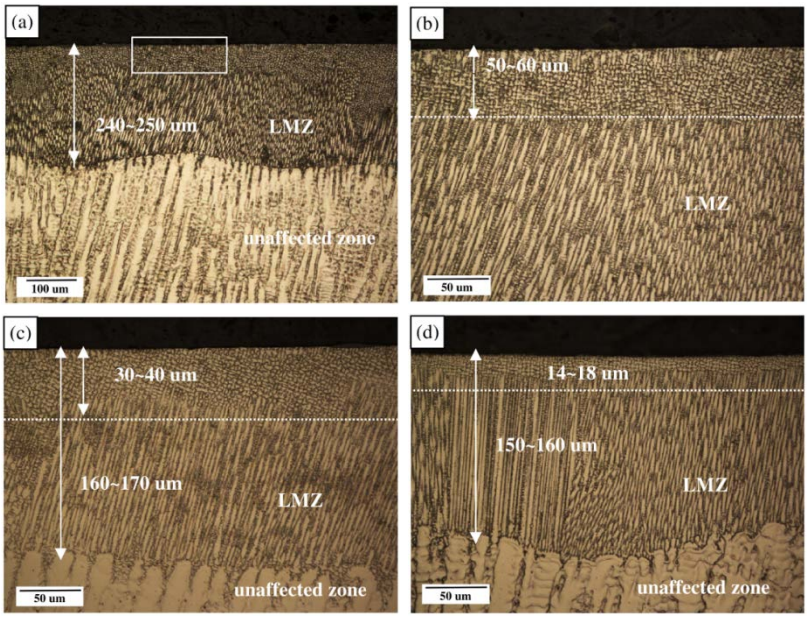

Fig. 12 Optical photographs showing cross-sectional microstructures of LSM specimens: (a) LSM-0.8 specimen; (b) high-magnification view of boxed region in (a); (c) LSM-1.0 specimen; (d) LSM-1.2 specimen.

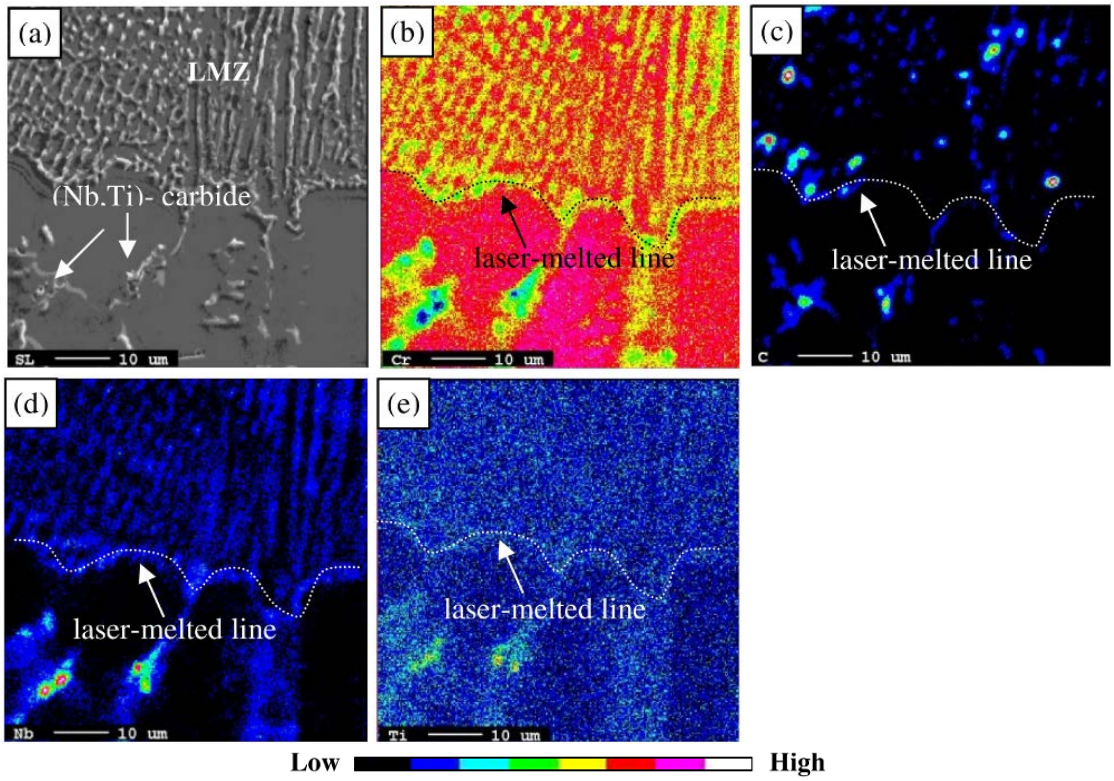

Fig. 13 EPMA results for cross-section of LSM-0.8 specimen: (a) SEM image; (b)-(e) Cr, C, Nb and Ti element mappings, respectively.

Figure 14 shows the DL-EPR curves of the LSM-0.8, LSM-1.0 and LSM-1.2 specimens. It is observed that none of the specimens experience anodic dissolution during the reactivation scan. For all of the samples, the passive current is almost the same as that for the AW specimen. In addition, the DOS value is again equal to zero. In other words, the LSM treatment effectively improves the corrosion resistance of the sensitized Alloy 82 weld.

Figure 15 presents optical micrographs of the three LSM specimens following the DL-EPR tests. The images show signs of only slight pitting corrosion (see Figs.15a), which is consistent with the absence of anodic dissolution during the reactivation scan (see Fig. 14). Figs. 15b show optical micrographs of the interface surface region between the LSM zone and the heat affected zone (HAZ) in the three samples. Comparing the three images, it is seen that the corrosion susceptibility of the HAZ increases with an increasing laser scanning speed. It may be attributed to the holding time (including heating and cooling times) is increased with the increase of scanning speed within the Cr-carbides precipitation temperature range. Nonetheless, the images confirm the effectiveness of the LSM process is restoring the passivation of the sensitized AW sample and improving the IGC resistance as a result.

Figs. 15c present cross-sectional optical micrographs of the three LSM samples. For each sample, the microstructure consists of a restored zone and an unaffected zone. In the unaffected zone, the corrosion activity is located mainly along the grain boundaries and spreads in the direction of the heat flow path (i.e., perpendicular to the substrate surface). However, in the restored zone, the passivation properties are regained and the IGC resistance enhanced due to the elimination of microstructural imhomogeneities and sensitized microstructures (e.g., Cr-depletion zones)

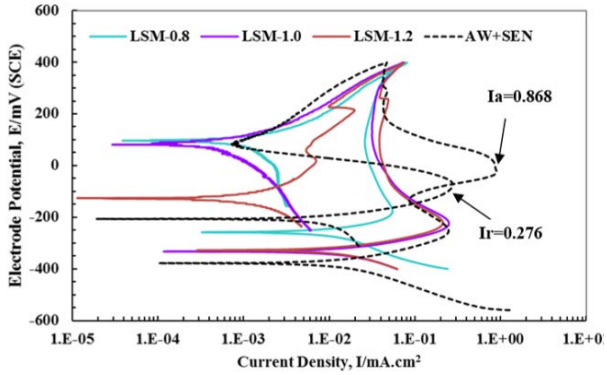

Fig. 14 DL-EPR polarization curves for LSM and AW+SEN specimen.

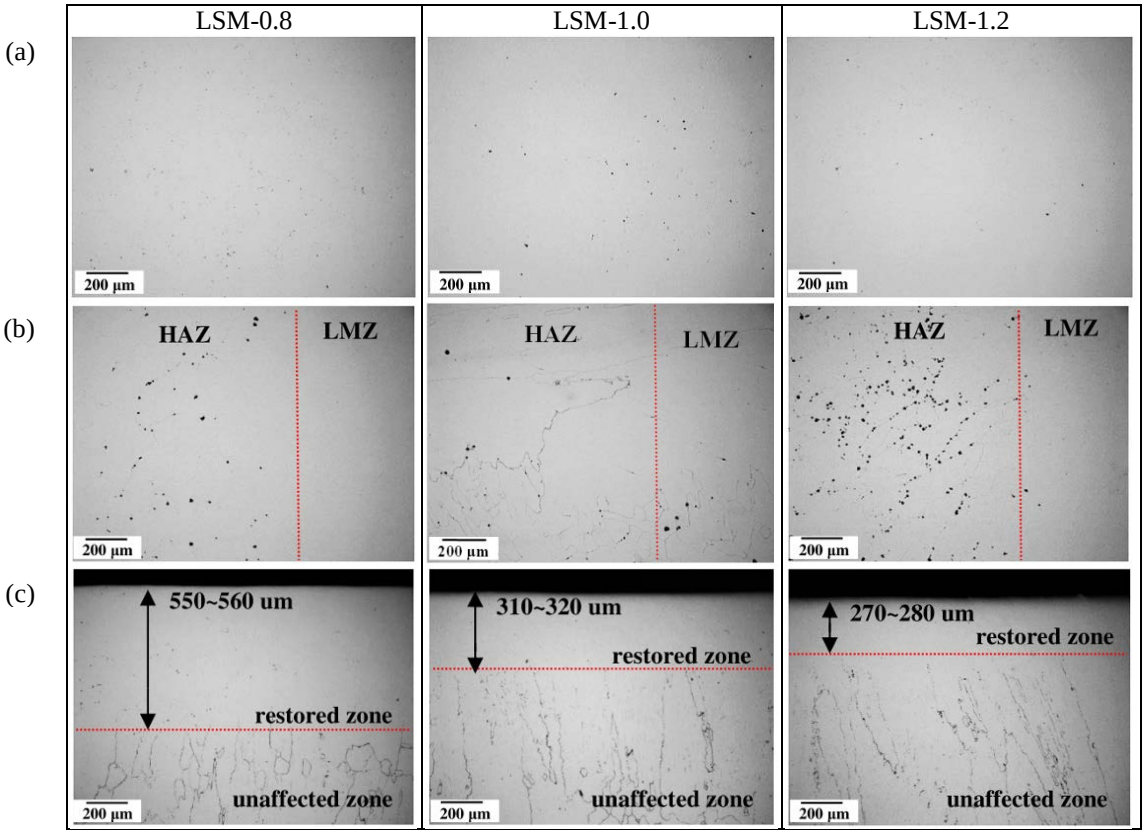

Fig. 15 Optical photographs of LSM specimens after DL-EPR tests; (a) surface micrographs; (b) surface micrographs including heat-affected zone (HTZ); (c) cross-sectional micrographs.

CONCLUSION

LSM treatment has been performed to recover the corrosion resistance of sensitized Alloy 82 welds. The experimental results support the following main conclusions:

The microstructures of Alloy 82 overlay weld comprised of cellular dendrite, which could be further refined by LSM treatment. MC (NbC,TiC) carbide was formed in the as-welded Alloy 82 deposit. The sensitization treatment at 650℃ for 24 hours enhanced the formation of fine and dense Cr-rich carbides mainly along the subgrain boundaries. LSM treatment could cause the partial dissolution of those fine precipitates presented in the SEN specimen into the matrix.

The preferential dissolution at the interfaces between distinct precipitates and the austenite matrix, which could be located intra- and inter-granularly, was responsible for the degradation of corrosion resistance of all the weld overlays. Numerous precipitates formed in the AW+SEN specimen resulted in a high DOS value and severe corrosion in the potentiostatic test. An improvement in IGC resistance of the overlay weld after LSM treatment was associated with a great reduction of harmful precipitates mainly at the subgrain boundaries of AW+SEN specimen.

REFERENCES

Bao, G., Shinozaki, K., Iguro, S., Inkyo, M., Yamamoto, M., Mahara, Y., and Watanabe, H., "Stress corrosion cracking sealing in overlaying of Inconel 182 by laser surface melting," J. Mater. Process. Technol., Vol. 173, No. 3, pp. 330-336(2006).

Bao, G., Yamamotoa, M., and Shinozakia, K., "Precipitation and Cr depletion profiles of Inconel 182 during heat treatments and laser surface melting," J. Mater. Process. Technol., Vol. 209, pp. 416-425(2009).

Briant, C.L., and Hall, E.L., "Intergranular corrosion of high chromium nickel-base alloys," Corrosion, Vol. 43, No. 7, pp. 437-440(1987).

Briant, C.L., and Hall, E.L., "The microstructural causes of intergranular corrosion of Alloys 82 and 182," Corrosion, Vol. 43, No. 9, pp. 539-548(1987).

Celin, R., and Tehovnik, F., "Degradation of a Ni-Cr-Fe alloy in a pressurised water nuclear power plan," Mater. Technol., Vol. 45, No. 2, pp. 151–157(2011).

Cihal, V., "A potentiokinetic reactivation method for predicting the I.C.C. and I.G.S.C.C. sensitivity of stainless steels and alloys," Corros. Sci., Vol. 20, No. 6, pp. 737-744(1980).

Chu, H.A., Young, M.C., Chu, H.C., Tsay, L.W., and Chen, C., "Hot cracking susceptibility of Alloy 52M weld overlays onto CF8 stainless steel," J. Nucl. Mater., Vol. 433, pp. 419-423(2013).

Fang, Z., Zhang, L., Wu, Y.S., Li, J.Q., Sun, D.B., Jiang, G. and Cui, Z.M., "Thioacetamide as an activator for the potentiodynamic reactivation method in evaluating susceptibility of type 304L stainless steel to intergranular corrosion," Corrosion, Vol. 51, No. 2, pp. 124-130(1995).

Hamada, I., and Yamauchi, K., "Intergranular corrosion resistance of Ni-Cr-Fe Alloy 82 weld metals overlaid on a low-alloy steel with wide-strip electrodes," Corrosion, Vol. 59, No. 2, pp. 181-188(2003).

Kasparova, O.V., "Intergranular corrosion of nickel alloys (review)," Prot. Met., Vol. 36, No. 6, pp. 524–532(2000).

Lee, H.T., and Kuo, T.Y., "Effects of niobium on microstructure, mechanical properties, and corrosion behavior in weldments of alloy 690," Sci. Technol. Weld. J., Vol. 4, No. 4, pp. 246-256(1999).

Lee, H.T., and Jeng, S.L., "Characteristics of dissimilar welding of alloy 690 to 304L stainless steel," Sci. Technol. Weld. J., Vol. 6, No. 4, pp. 225-234(2001).

Lee, H.T., and Wu, J.L., "Intergranular corrosion resistance of nickel-based alloy 690 weldments," Corros. Sci., Vol. 52, pp. 1545-1550 (2010).

Lee, H.T., and Liu, T.C., "The improvement of corrosion resistance of sensitized Alloy 82 welds using laser surface melting," Mater. Trans., Vol. 58, No. 9, pp. 1329-1336(2017).

Lim, Y.S., Suh, J.H., Kuk, I.H., and Kim, J.S., "Microscopic investigation of sensitized Ni-base alloy 600 after laser surface melting," Metall. Mater. Trans. A, Vol. 28, pp. 1223-1231 (1997).

Lim, Y.S., Kim, H.P., Han, J.H., Kim, J.S., and Kwon, H.S., "Influence of laser surface melting on the susceptibility to intergranular corrosion of sensitized Alloy 600," Corros. Sci., Vol. 43, pp. 1321-1335(2001).

Lim, Y.S., Kim, J.S., Kim, H.P., and Cho, H.D., "The effect of grain boundary misorientation on the intergranular $M_{23}C6$ carbide precipitation in thermally treated Alloy 690," J. Nucl. Mater., Vol. 335, pp. 108-114(2004).

Liu, C., Huang, H., and Che, S., "Activators for EPR test in detecting sensitization of stainless steels," Corrosion, Vol. 48, No. 8, pp. 686-690(1992).

McCracken, S.L., and Smith, R.E., "Behavior and hot cracking susceptibility of filler metal 52 M (ERNiCrFe-7A) overlays on cast austenitic stainless steel base materials, Hot Cracking Phenomena in Welds III, Springer Berlin Heidelberg, pp. 333-352(2011).

Mudali, U.K., Dayal, R.K., Gnanamoorthy, J.B., Kanetkar, S.M., and Ogale, S.B., "Localized corrosion studies on laser surface melted type 316 austenitic stainless steel," Mater. Trans. JIM, Vol. 32, No. 9, pp. 845-853(1991).

Peng, Q.J., Yamauchi, H., and Shoji, T., "Investigation of dendrite-boundary microchemistry in alloy 182 using auger electron spectroscopy analysis," Metall. Mater. Trans. A, Vol. 34, pp. 1891-1899(2003).

Sennour, M., Chaumun, E., Crépin, J., Duhamel, C., Gaslain, F., Guerre, C., and de Curières, I., "TEM investigations on the effect of chromium content and of stress relief treatment on precipitation in Alloy 82," J. Nucl. Mater., Vol. 442, pp. 262-269 (2013).

Shin, J.K., Suh, J.H., Kim, J.S., and Kang, S.J. "Effect of laser surface modification on the corrosion resistance of Alloy 600," Surf. Coat. Technol., Vol. 107, pp. 94-100(1998).

Sindo Kou, WELDING METALLURGY, John Wiley & Sons, Inc., pp. 174-176(2003).

Suh, J.H., Shin, J.K., Kang, S.J., Lim, Y.S., Kuk, I.H., and Kim, J.S., "Investigation of IGSCC behavior of bensitized and laser-surface-melted Alloy 600," Mater. Sci. Eng. A, Vol. 254, No. 1-2, pp. 67-75(1998).

Tsai, W.T., Yu, C.L., and Lee, J.I., "Effect of heat

treatment on thesensitization of Alloy 182 weld," Scri. Mater., Vol. 53, pp. 505-509(2005).

Alloy 82 銲道微結構與沿晶腐蝕阻抗之研究

李驊登　劉得成
國立成功大學機械工程研究所

摘要

本研究探討晶界特性和敏化程度對Alloy 82覆銲層沿晶腐蝕性質的影響。以傳統電弧銲接製備之銲道組織具有67.9% 和212.4 cm/cm^{2}高角度晶界(大於15度以上)，在銲後熱處理，使富鉻碳化物於晶界析出，鄰近基材形成缺鉻區。經電化學測試結果，敏化值達31%，腐蝕形貌為沿晶腐蝕及晶粒內孔蝕；使用雷射表面重熔技術，將富鉻碳化物重熔回基材並抑制其再度析出，明顯提升抗腐蝕能力。